INTERNATIONAL JOURNAL OF HYDROGEN ENERGY 43 (2018) 5048–5067

Available online at www.sciencedirect.com

ScienceDirect

journal homepage: www.elsevier.com/locate/he

One-dimensional metal-hydride tank model and simulation in Matlab–Simulink

Z. Abdin, C.J. Webb, E.MacA. Gray *

School of Natural Sciences and Queensland Micro- and Nanotechnology Centre, Griffith University, Nathan 4111, Australia

ARTICLE INFO

Article history:
Received 25 September 2017
Received in revised form
11 January 2018
Accepted 17 January 2018
Available online 15 February 2018

Keywords:
Metal-hydride
Hydride tank
Model
Kinetics
Effective thermal conductivity

ABSTRACT

A model has been developed for a metal-hydride tank for hydrogen storage, based on linked modular mathematical models in Simulink®. The objective of the work was a tank-level model suitable for incorporation into a whole-of-system model, implying modest computing demands and reduced complexity. Finite-element analysis was not used. Because the apparent kinetics of a practicable metal-hydride tank is dominated by heat flow originating in the enthalpy of hydrogen absorption/desorption, particular attention was paid to modelling the effective thermal conductivity, based on a detailed description of the thermal resistance between hydride particles. The model was tested against our own experimental data for a pair of tanks with 6.4 kg total hydrogen capacity, and compared with a published 2D model and published experimental data. In all cases, the new model performed very well. The incorporation of a physical model of the effective thermal conductivity means that the tank model can also be used as a research tool to investigate ways of improving tank performance by altering the physical characteristics of the metal-hydride itself to achieve an optimal thermal design and enhanced reaction kinetics.

Introduction

Hydrogen storage is a key enabling technology for the advancement of hydrogen and fuel cell technologies in applications including stationary power, portable power, and transportation. Relative to other fuels, hydrogen has a very high gravimetric energy density (120 MJ kg^{-1} LHV) but a very low volumetric energy density at ambient temperature and pressure (96.4 MJ m^{-3} LHV). To match the gravimetric and volumetric energy densities of gasoline (44 MJ kg^{-1} and 32 GJ m^{-3} respectively), a hydrogen fuel tank would need to contain 35 mass% hydrogen compressed to 4 times liquid density.

The storage problem has been resolved in commercially available fuel-cell electric vehicles by compressing gaseous hydrogen to 70 MPa for small vehicles and 35 MPa for buses. This solution is unlikely to be feasible for larger storage units (say >100 kg H_2), however, because of high cost and low volumetric density.

While solid-state hydrogen storage achieves gravimetric energy densities that are unacceptably low for use in automobiles, it can achieve high volumetric energy density at near-ambient pressures [1]. Nickel-metal hydride batteries were the first commercial success for solid-state hydrogen storage [2]. Metal-hydride energy storage is beginning to be used in public off-grid buildings *e.g.* the Sir Samuel Griffith Centre, Griffith University, Brisbane, Australia [3], with 120 kg

* *Corresponding author.*
E-mail address: e.gray@griffith.edu.au (E.MacA. Gray).
https://doi.org/10.1016/j.ijhydene.2018.01.100

Glossary

a_H	Hertzian contact radius, m
a_L	Radius of macro-contact, m
b	Specific gas constant
c	Vickers microhardness coefficient
C_p	Specific heat capacity, J kg^{-1} K^{-1}
D	Diameter, m
d_v	Indentation diagonal depth, m
E	Activation Energy, kJ mol^{-1}
E'	Effective elastic modulus, GPa
F_n	Force, N
F	Reacted fraction
H/M	Hydrogen to metal ratio per formula unit or per metal atom; *i.e.* [0–6] or [0–1] for $LaNi_5$
H_v	Vickers microhardness, GPa
H_c	Contact microhardness, GPa
h_f	Heat transfer coefficient of fluid, W M^{-2}
k_B	Boltzmann constant, 1.38×10^{-23} J K^{-1}
k	Thermal conductivity, W m^{-1} K^{-1}
Kn	Knudsen number
K_r	Reaction rate coefficient
κ	Rate constant
K_p	Permeability, m^2
LHV	Lower heating value
l_m	Molecular mean-free path
$\dot{m}$	Rate of mass absorbed or desorbed, kg m^{-3}
M	Gas parameter
N	Coordination number
Nu	Nusselt number
n	Pre-exponential factor
s	Solid
p	Particle
eff	Effective
eq	Equilibrium
in	Initial
ref	Reference
sat	Saturation
su	Supply
tn	Tank
P	Pressure, Pa
Pr	Prandtl number
r	Radial coordinate, m
R_g^*	Universal gas constant, 8.3144 J mol^{-1} K^{-1}
Re	Reynolds number
R	Radius of sphere, m
R_c	Thermal contact resistance, Ω
R_s	Micro-contact thermal resistance, Ω
R_L	Macro-contact thermal resistance, Ω
R_g	Micro-gap thermal resistance, Ω
R_G	Macro-gap thermal resistances, Ω
T	Temperature, K
V	Volume, m^3
ρ	Density, kg m^{-3}
v	Velocity, m s^{-1}
ε	Porosity
t	Time, s
w	Weight percent, %
τ	Ratio of expansion
σ	Surface roughness, m
α_T	Thermal accommodation coefficient
γ	Adiabatic exponent
μ	Dynamic viscosity, kg m^{-1} s^{-1}

Subscripts

a	Absorption
d	Desorption
f	Fluid
g	Gas

H_2 capacity (≈2 MW-h electric equivalent) and the Henn-na Hotel, Nagasaki, Japan [4].

The advantages of metal-hydride storage in these situations come from (i) the decoupling of power and energy ratings, which makes it advantageous for long-term storage compared to batteries [5]; (ii) its ability to be tuned for low operating pressure suitable for direct coupling to an electrolyser (~1 MPa); (iii) excellent safety coming from the low pressure and relatively slow kinetics of hydrogen release; and (iv) high volumetric energy density. For example, the classic intermetallic hydride $LaNi_5H_6$ contains only 1.4 mass% hydrogen, but has a 100%-dense volumetric capacity of approximately 115 kg m^{-3} at room temperature and <1 MPa pressure [6] compared to 70.8 kg m^{-3} at 20.3 K and 0.1 MPa for liquid hydrogen.

The design of a system involving any modality of hydrogen storage requires modelling of its characteristics and interactions with the rest of the energy system. Modelling hydrogen storage in a metal hydride (MH) is a complex multi-physics problem, which involves compressible gas flow in a porous MH bed, coupled with heat transfer and reaction kinetics. For example, the enthalpy of formation of $LaNi_5H_6$ is ≈30 kJ mol^{-1}, so charging 1 kg of hydrogen releases ≈15 MJ of heat, compared to the stored energy of 120 MJ LHV. This heat must be managed, preferably via thermal storage and use in another process. The key point from the modelling perspective is that the effective thermal conductivity of MH beds is very poor owing to their porosity and inter-particle contact resistance. Various values have been reported for the measured effective thermal conductivity of a $LaNi_5$ powder bed (with porosity ≈0.5), the most reliable representative value probably being 1.32 W m^{-1} K^{-1} [7], compared to >30 W m^{-1} K^{-1} for a solid composite compact of $LaNi_5$ [8]. As a result of the poor thermal conductivity, the observed reaction kinetics for absorption and desorption of hydrogen is dominated by heat flow [9]. Realistic thermal modelling, especially of the thermal conductivity, is therefore essential to build a quantitative model of MH storage.

This paper continues a series in which mutually compatible modular models of the components of an energy system, specifically one incorporating solar-derived hydrogen [3], are presented. One overall objective is to link the suite of component models together to form a whole-of-system model and simulation that can realistically predict the behaviour of a

planned energy system, as a prerequisite to specifying the characteristics and capacities (sizes) of its components. An accurate and efficient model can also be applied to simulate the behaviour of an existing energy system, for example on-the-fly prediction of the trajectory of the energy system as its input(s) and load(s) change in real time. The component models are realised in Simulink®. The first three such models are for a PEM electrolyser cell [10], a PEM fuel cell [11] and a KOH electrolyser cell [12]. The next, for a MH tank, is presented here.

A second objective of the work is to build component models capable of use as research tools to predict the effects of influential design parameters, materials and environmental conditions, thus lessening the need for experimentation and prototyping, which is expensive and time-consuming.

Design parameters are necessarily physical in nature, meaning related to dimensions, materials properties, *etc.*, and should appear in any theory that represents measurable reality. On the other hand, many presently available models in this field take a semi-empirical approach, representing the characteristics of the MH tank through equations containing empirical terms and coefficients that lack any direct relationship to physical reality [13,14]. This creates a disconnect between design and measured performance. The key to achieving the second objective is therefore to place the equations that embody the characteristics of the various elements of the electrolyser, MH tank, fuel cell *etc.* on a proper physical basis by embedding the theory of the underlying physical mechanisms. Doing this has significant advantages. Firstly, it makes the model more widespread in its application, in contrast to the present general reliance on empirical equations that only describe the characteristics of the particular component under consideration, perhaps with no applicability to the greater class of such components. Secondly, a sound physical basis for the model better allows the effects of changing materials, dimensions *etc.* to be predicted in the quest for enhanced performance, by performing sensitivity analyses, for instance. Thirdly, a realistic physically-based model may potentially be used to diagnose problems in the modelled component or system via changes in the fitted parameters arising from, for instance in the present case, compaction following absorption–desorption cycling modifying the effective thermal conductivity of the MH bed.

Generally, a multi-dimensional finite-element model is useful to understand the details of the individual components of a MH tank in order to optimise the mechanical and thermal design, but for simulating an entire hybrid energy system it would be unworkable. An important question to be answered by this study was whether a model simplified sufficiently to be viable in a real-time simulation environment could have acceptable accuracy.

A detailed 1D dynamic model for a MH tank has been developed and tested against experimental results and published models. The requirement was for a MH tank model suitable for incorporation into a whole-of-system model, implying modest computing demands and reduced complexity. On-the-fly finite-element analysis is impracticable in this scenario. This necessitated direct numerical solution of the governing equations in the minimum number of dimensions. A one-dimensional model was therefore built and tested using data for MH tanks with axial symmetry. The computational demands are small enough for it to be embedded in a whole-of-system model and simulation. The approach adopted insists on a physical basis for the model parameters wherever feasible. The effective thermal conductivity has been modelled for a randomly structured packed bed consisting of uniformly sized spheres immersed in gas, including, the thermal contact resistance between spheres. The physically based parameterisation of the model exposes the relative contributions of the various parameters to the heat and mass transfer rates of the MH bed in detail. The model was successfully tested against data from a pair of real MH tanks with 6.4 kg H_2 hydrogen storage capacity.

Review of recent modelling approaches

The history of MH tank modelling up to 2015, and the advantages and disadvantages of various conceptual approaches to MH tank modelling, have been discussed and reviewed by Mohammadshahi et al. [15]. The latest developments are briefly surveyed here. The key factors determining the usability of a model within a whole-of-system simulation are the methodology applied, the complexity of the internal structure and the model adopted for effective thermal conductivity of the MH bed. The representation of the pressure-composition-temperature relationship for the material of the MH bed is also an important factor, but the requirement is for a sufficiently accurate equation, which will probably vary strongly between materials and can anyway be solved numerically on-the-fly with modest computing resources. The models surveyed are summarised in Table 1.

Methodology

A mathematical model was developed by Mellouli et al. [16] to study the 2D coupled heat and mass transfer inside a hydride bed coupled to a phase-change material for storing heat, using ANSYS Fluent. The model was used to compare cylindrical and spherical tanks, the latter exhibiting superior performance. Mohammadshahi et al. [17] [18], developed a 3D model with an improved approach in COMSOL Multi-physics, based on the Hardy and Anton model [19]. They explored the effects of various parameters on MH tank performance and applied their model to a full absorption–desorption cycle for which the conditions at the end of the cycle were constrained to be the same as at the start. Mohammadshahi et al. [20] also tested their model using measurements of the local hydrogen concentration obtained by volume-resolved neutron powder diffraction. Kyoung et al. [21] developed a 3D MH tank model in computational fluid dynamics (CFD) for studying the reaction kinetics and heat and mass transfer mechanisms during the hydrogen desorption process. Sekhar et al. [22] demonstrated a 3D numerical model of heat and mass transfer for comparing H_2 uptake performances using different heat exchangers. Darzi et al. [23] used a 2D model to investigate the cooling and heating of a cylindrical $LaNi_5$ MH tank using an annular jacket filled with phase-change material. Valizadeh

Table 1 – Summary of published models.

Ref.	Model type	Solution methods	MH bed	Heat exchanger	Porosity calculation	Effective thermal conductivity calculation (W m^{-1} K^{-1})	Model for Absorption/ desorption	Equilibrium Pressure calculation
[21]	3D	CFD *i.e.* STAR-CD	$LaNi_5$	External thermostatic bath	0.63	$\lambda_{eff} = \varepsilon\lambda_g + (1-\varepsilon)\lambda_s$	Desorption	$P_{eq} = \left(a_o + \sum_{n=1}^{9} a_n \left(\frac{H}{M}\right)^n\right) \exp\left(\frac{\Delta H}{R_g}\left(\frac{1}{T} - \frac{1}{T_{ref}}\right)\right)$
[22]	3D	COMSOL Multiphysics	$MmNi_{4.6}Al_{0.4}$	axial tubing, coiled tubing, transversal fins	0.52/0.40	–	Both	Ref. [29]
[30]	3D	C^{++} and gPROMS	$LaNi_5$	External thermostatic bath	0.50	$k = \begin{cases} k_1 \\ k_2 \\ 2k_1k_2/k_1 + k_2 \end{cases}$	Absorption	$P_{eq} = f\left(\frac{H}{M}\right) \exp\left(\frac{\Delta H}{R_g}\left(\frac{1}{T_0\theta} - \frac{1}{T_{ref}}\right)\right)$
[31]	3D	FVM, SIM-PLE algorithm	$LaNi_5$	External thermostatic bath	0.3	1.32	Absorption	$\ln P_{eq} = A - B/T$
[32]	3D	FEM (COMSOL Multiphysics)	$LaNi_5$	Concentric finned multi tubular	0.5	1.32	Absorption	$P_{eq} = \sum_{i=0}^{7} a_i X_i \exp\left(\frac{\Delta H}{R_g}\left(\frac{1}{T_s} - \frac{1}{303}\right)\right)$
[19]	2D & 3D	FEM (COMSOL Multiphysics)	$NaAlH_4$	tube and fin heat exchanger	0.7	–	Both	$P_{eq}\,(T) = 10^5 \exp\left[\frac{\Delta H}{RT} - \frac{\Delta S}{R}\right]$
[17]	3D	FEM (COMSOL Multiphysics)	$LaNi_5$	Concentric fin tube	$\varepsilon = E_p\,(1-\varepsilon_i)$ $\eta + \varepsilon_i$	$\lambda_{eff} = \frac{B_1 P^{B_2}}{1/B_0 + P^{B_2}}$	Both	$P_{eq} = \left[\frac{C_0 C_1 \eta^{C_2}}{1+C_1\eta^{C_2}} + C_3\eta + e^{C_4(\eta - C_5)}\right] \exp\left[-K\left(\frac{1}{T} - \frac{1}{T_{ref}}\right)\right]$
[24]	2D	LBM	$LaNi_5$	External thermostatic bath	0.5	$\lambda_{eff} = \varepsilon\lambda_g + (1-\varepsilon)\lambda_s$	Desorption	$\ln\left(\frac{P_{eq}}{P_{ref}}\right) = A - B/T$
[16]	2D	Fluent 6.3.26	Mg	PCM	0.4	–	Both	$\ln\left(\frac{P_{eq}}{P_{ref}}\right) = \frac{\Delta H}{RT} - \frac{\Delta S}{R_g}$
[25]	2D	ANSYS Fluent	$LaNi_5$	heat pipes	0.5	1.32	Both	Ref. [25]
[33]	2D	FEM (COMSOL Multiphysics)	MOF-5 Pellet	ENG	$\varepsilon_g = \varepsilon_{tot} - \rho_p v_a$	$\lambda_{ax} = \sum_{i=1}^{4} l_i T^{i-1}$	Absorption	$P_{eq} = q^* = M_{H_2} {}^* \eta_{abs} = \frac{M_{H_2}\eta_{max} RT}{E_{max} - E_{min}} \ln\left[\frac{a+p\,\exp(E_{max}/RT)}{a+p\,\exp(E_{min}/RT)}\right]$
[14]	2D	CVFEM/semi analytical	$LaNi_5$	Concentric finned tube	0.5	$\lambda_{eff} = \varepsilon\lambda_g + (1-\varepsilon)\lambda_s$	Absorption	$\ln P_{eq} = \frac{\Delta H}{RT} - \frac{\Delta S}{R_g}$
[25]	2D	ANSYS Fluent	$LaNi_5$	Heat pipe, Metal rod	0.5	1.32	Both	Absorption: $\ln\left(\frac{P_{eq}}{P_{ref}}\right) = (A_a - B/T + a.H/M_{0.3\ wt\%}) \times \left[1 - \frac{(H/M - H/M_{\vert 0.3\ wt\%})^2}{(H/M_{emp} - H/M_{\vert 0.3\ wt\%})^2}\right],\ H/M < H/M_{\vert 0.3\ wt\%}$ $\ln\left(\frac{P_{eq}}{P_{ref}}\right) = (A_a - B/T + a.H/M),\ H/M_{\vert 0.3\ wt\%} \le H/M \le H/M_{\vert 1.1\ wt\%}$

(*continued on next page*)

Table 1 – (*continued*)

Ref.	Model type	Solution methods	MH bed	Heat exchanger	Porosity calculation	Effective thermal conductivity calculation ($W\ m^{-1}\ K^{-1}$)	Model for Absorption/ desorption	Equilibrium Pressure calculation
								$\ln\left(\frac{P_{eq}}{P_{ref}}\right) = (A_a - B/T + a.H/M_{\|1.1\ wt\%}) + \frac{b}{T}(H/M - H/M_{\|1.1\ wt\%})^2$, $H/M_{\|1.1\ wt\%} \le H/M$
								Desorption:
								$\ln\left(\frac{P_{eq}}{P_{ref}}\right) = (A_d - B/T + a.H/M_{\|0.3\ wt\%}) \times\left[1 - \frac{(H/M - H/M_{\|0.3\ wt\%})^2}{(H/M_{emp} - H/M_{\|0.3\ wt\%})^2}\right],\ H/M < H/M_{\|0.3\ wt\%}$
								$\ln\left(\frac{P_{eq}}{P_{ref}}\right) = (A_d - B/T + a.H/M),\ H/M_{\|0.3\ wt\%} \le H/M \le H/M_{\|1.1\ wt\%}$
								$\ln\left(\frac{P_{eq}}{P_{ref}}\right) = (A_d - B/T + a.H/M_{\|1.1\ wt\%}) + \left(D + \frac{b}{T}\right)(H/M - H/M_{\|1.1\ wt\%})^2$, $H/M_{\|1.1\ wt\%} \le H/M$
[7]	2D	CVFEM	$LaNi_5$	Cooling fluid	0.5	1.32	Absorption	$P_{eq} = f\left(\frac{H}{M}\right)\exp\left(\frac{\Delta H}{R_g}\left(\frac{1}{T} - \frac{1}{T_{ref}}\right)\right)$
[34]	2D	FVM/Fluent	$LaNi_5$	Forced air/liquid cooling	0.3	1.25	Absorption	$P_{eq} = P_{eq}^{ref}\ \exp\left(-\frac{\Delta H}{R}\left(\frac{1}{T} - \frac{1}{T_{ref}}\right)\right)$
[35]	2D	FEM	$LaNi_5$	Cooling fluid	0.63	1.087	Both	$P_{eq} = f\left(\frac{H}{M}\right)\exp\left(\frac{\Delta H}{R_g}\left(\frac{1}{T} - \frac{1}{T_{ref}}\right)\right)$
[36]	2D	PHOENICS	$LaNi_5$	Cooling fluid	0.5	1.27	Absorption	$\ln P_{eq} = A - B/T$
[37]	2D	FVM	IRH3 activated carbon	Natural air	0.88	0.2	Absorption	$q_{eq} = q_0\ \exp\left[-\left(\frac{RT}{E_a}\ln\left(\frac{P_{lim}}{P}\right)\right)^2\right]$
[13]	2D	FEMLAB	$LaNi_5$	External fin	0.5	1.32	Both	$\ln P_{eq} = A - B/T$
[7]	2D	CVFEM	$LaNi_5$	Cooling fluid	0.5	1.32	Both	$P_{eq} = f\left(\frac{H}{M}\right)\exp\left(\frac{\Delta H}{R_g}\left(\frac{1}{T} - \frac{1}{T_{ref}}\right)\right)$
[38]	2D	FEM (Comsol Multiphysics)	$MmNi_{4.6}Al_{0.4}$	Cooling jacket/ tubes	0.5	1.62	Absorption	$P_{eq} = 10^5\ \exp\left[\frac{\Delta S}{R_u} - \frac{\Delta H}{R_u T} + (\varphi + \varphi_0)\tan\left[\pi\left(\frac{c}{c_f} - \frac{1}{2}\right) + \frac{\beta}{2}\right]\right]$

[39]	2D	PHOENICS	$LaNi_{4.8}Sn_{0.2}$	Cooling fluid	0.55	1.6	Absorption	$\ln P_{eq} = A - B/T$
[40]	2D	FEM (Comsol Multiphysics)	AB5 type MH	Circulating water tube	0.5	$\lambda_{mh} = 0.6 + 0.4F$	Both	$Peq = 10131.5 \exp\left[\left(a - \frac{b}{T_{mh}}\right) + (c \pm d)\tan\left\{\pi\left(\frac{F}{x_0}\right)\right\} \pm \frac{e}{2}\right]$, $x_0 = \frac{1}{\exp\left(f - \frac{g}{T_{mh}}\right)}$
[23]	2D	Fluent™	$LaNi_5$	Annular jacket with PCM	0.4, 0.5, 0.6	$k_{eff} = \varepsilon k_g + (1 - \varepsilon)k_s$	Both	$\ln\left(\frac{P_{eq}}{P_{ref}}\right) = A - B/T$
[41]	2D	FEM (Comsol Multiphysics)	$LaNi_5$	Metal foam and concentric tube with fluid	0.55	$k_{eff} = k_{foam} + \varepsilon_{foam} k_{MH} + \varepsilon_{foam}\varepsilon_{MH} k_{H_2}$	Absorption	$P_{eq} = f\left(\frac{H}{M}\right)\exp\left(\frac{\Delta H}{R_g}\left(\frac{1}{T} - \frac{1}{T_{ref}}\right)\right)$
[42]	2D	CVM	$LaNi_5$	Thermostatic bath	$\varepsilon = 1 - (1 - E_p\eta)(1 - \varepsilon_0)$	$k_{eff} = \varepsilon k_g + \frac{0.895(1-\varepsilon)}{\phi + (2k_g/3k_s)} k_g$	Both	In the plateau region: $P_{eq} = (B_1 + B_2X + B_3X^3 + B_4X^4) f(T)$ $X_{pl,min} < X < X_{pl,max}$ In other regions: $P_{eq} = (A_1 + A_2X + A_3X^2 + A_4X^3 + A_5X^4 + A_6X^5) f(T)$ $X < X_{pl,min}$ and $X_{pl,max} < X$ $f(T) = C_1 + C_2T + C_3T^2 + C_4T^3$
[26]	1D & 2D	ANES, SIMPLE	$LaNi_5$	Aluminium foam	0.55	$\lambda_{eff} = \frac{\lambda_g}{\varepsilon^3}$, 10.9	Both	Ref. [41]
[27]	1D	Dymola®	$Ti_{1.1}CrMn$	U-tube configuration embedded in the solid bed	0.6	1	absorption	$P_{eq} = P_0 \exp\left(\frac{\Delta H}{RT} - \frac{\Delta S}{R}\right)$
[43]	1D	FEM (Comsol Multiphysics)	$La_{0.83}Ce_{0.10}Pr_{0.04}Nd_{0.03}Ni_{4.4}Al_{0.60}$	Water bath	0.5	1.5	Both	$\ln P = \ln P_0 + 2\ln\left(\frac{\theta}{1-\theta}\right) - \frac{27}{2}\frac{T_c}{T}\theta + 2\frac{\theta}{1-\theta}$
[44]	1D	Finite volume FTCS	$Zr_{0.9}Ti_{0.1}Cr_{0.55}Fe_{1.45}$	External fin	0.25	5	Both	$\ln\frac{P_{eq}}{P_r} = \frac{\Delta H}{RT} - \frac{\Delta S}{R} + \Delta\ln P\frac{(X - X_\alpha)}{(X_\beta - X_\alpha)} + \ln\left(\frac{P_a}{P_d}\right)$
[45]	1D	FDM	$LaNi_5$	Aluminium foam	0.55	$k_{eff} = k_{foam} + \varepsilon_{foam} k_{MH} + \varepsilon_{foam}\varepsilon_{MH} k_{H_2}$	Both	$\ln\left(\frac{P_{eq,r}}{1atm}\right) = \frac{\Delta H_r}{R_g T} - \frac{\Delta S_r}{R_g} + g_r\left(x_H - \frac{1}{2}\right)$
[46]	1D	Matlab/Simulink	Hydralloy C5 metal hydride	Water bath/natural air	–	1	Both	$\ln P_{eq} = \frac{\Delta H}{RT} - \frac{\Delta S}{R_g}$
[29]	0D	Matlab/Simulink	$LaNi_5$	Circulating fluid	0.5	1.32	Desorption	$\ln\frac{P_{eq}}{P_0} = a - \frac{b}{T} + (\phi \pm \phi_0)\tan\left\{\alpha_1\pi\left(\left[\frac{H}{H_{max}}\right] - \alpha_2\right)\right\} \pm \frac{\beta}{2}$
[47]	–	4th order Runge–Kutta algorithm	$MmNi_{4,6}Fe_{0,4}$	Copper fins inside the bed	–	5.5	Both	$\ln\frac{P_{eq}}{P_0} = \frac{\Delta H}{RT} - \frac{\Delta S}{R} + f_{slope}(X - X_m) + f_{hys}$

et al. [24] developed a 2D mathematical model to evaluate the transient heat and mass transfer for hydrogen desorption, and simulations were performed by the Lattice Boltzmann method. Chung et al. [25] used ANSYS Fluent to develop a 2D model to predict hydrogen storage performance and coolant behaviour. The model was applied to tank designs with and without heat pipes and internal fins. Minko et al. [26] developed a multi-dimensional model to visualise the heat and mass transfer processes in a MH reactor with aluminium foam. A 1D model to predict the weight fraction of the absorbed hydrogen and the MH bed temperature was developed by Mazzucco and Rokni [27]. The heat exchanger was U-shape aluminium coolant tube embedded in the MH bed with axial symmetry. The great majority of published models are at least two-dimensional and based on finite-element analysis. Lowered symmetry and end effects in cylindrical MH beds are the main reasons for modelling in more than one dimension. Yet many literature reports do concern tanks whose symmetry is cylindrical or nearly so. A long cylinder with axial internal symmetry should not require modelling in more than one dimension and may therefore be amenable to numerical techniques that do not require finite-element analysis. An interesting question is whether a tank with lower internal symmetry can nevertheless be modelled in one dimension through a modification to the model of effective thermal conductivity.

Effective thermal conductivity

The apparent kinetics of the MH tank depends strongly on the heat transfer characteristics of the MH bed, and without effective heat exchange to remove/add the enthalpy of absorption/desorption will reflect heat transfer almost entirely [9]. The effective thermal conductivity (ETC) is a lumped parameter usually employed to represent the heat transfer characteristics of the inhomogeneous MH bed. The ETC depends principally on the porosity and the inter-particle contact thermal resistance and generally varies with position in the bed through the inhomogeneous phase proportions of the concentrated and expanded metal-hydride phase. The ETC also varies with temperature and, owing to Knudsen flow through the void volume, pressure. As Table 1 shows, in many cases a constant value based on experiment has been adopted in modelling studies. This approach is unlikely to yield accurate results because of the listed dependencies.

The early history of ETC modelling and experimental work, the advantages and disadvantages of various conceptual approaches to ETC modelling, augmentation techniques and experimental work have been reviewed and discussed by Madaria et al. [28].

Model development

The real tank to be modelled (details in § New experiments) had no internal structure and essentially perfect cylindrical symmetry, with a surrounding annular cooling/heating jacket. The entire tank, including the ends, was wrapped in thermal insulation, creating a pseudo-adiabatic external boundary. These features made it ideal for testing a 1D model.

Metal hydride basics

The reaction between a metal M and hydrogen may be represented as

$$\mathrm{M} + \frac{x}{2}\mathrm{H_2} \leftrightarrow \mathrm{MH}_x \tag{1}$$

where x is the hydrogen-to-metal atomic ratio, usually written H/M. On a mass basis, the amount of hydrogen taken up is

$$w = \frac{xM_H}{M_M + xM_H} \tag{2}$$

where M_M is the average atomic weight of the metal atoms and M_H is the atomic weight of H. If the maximum amount of hydrogen taken up is $[H/M]_{max}$ in atomic terms or $[w]_{max}$ in mass terms, the reacted fraction is defined as

$$F = \frac{H/M}{[H/M]_{max}} = \frac{w}{[w]_{max}} \tag{3}$$

The absorption/desorption of hydrogen takes place in a range of pressures, between limiting concentrations that correspond to the phase boundaries of the pure dilute (α) and the pure concentrated hydride (β) phases. In $LaNi_5H_x$ ($x \in [0, 6.7]$), for instance, at 300 K the α-phase limiting concentration is $x \approx 0.5$ and the β-phase limiting concentration is $x \approx 6.0$. Ideally, according to the Gibbs Phase Rule the phase conversion occurs over a plateau at constant pressure in the pressure–composition isotherm, but real hydrides exhibit plateau slope and pressure hysteresis. Phase conversion has an associated enthalpy which is released/absorbed between the phase boundaries, while little heat is released/absorbed when changing the concentrations of the dilute and concentrated pure phases. More detail may be found in the book by Fukai [48].

Model assumptions

The model assumed perfect cylindrical symmetry and axial variations were neglected. The latter assumption is equivalent to an adiabatic boundary condition at each end of the tank. This is reasonable in general for a cylindrical tank that is long relative to its diameter, and particularly so in the present case in which the heat exchanger surrounded only the cylindrical tank surface and the tanks ends were insulated. Consequently, heat and mass transfer were considered only in the radial direction.

The MH bed was assumed to be an isotropic and randomly packed structure of notionally identical rough spheres with local deviations from the average curvature. To model a random packed bed, it is generally assumed that the asperities deform plastically [49]. The assumption of monodispersivity has been discussed by Gusarov and Kovalev [50]. It is clear that a non-realistic assumption leads to errors in the computed effective thermal conductivity. In the approach adopted here, the distribution of sphere diameters is assumed to be less influential than the existence of micro-contacts between spheres, which are expected to mask the details of the gross particle geometry.

Within the MH bed, thermal energy can in principle be transferred between the solid particles by conduction through

the real contact area, conduction through the interstitial gas in the gaps between the particles, convection through the gas and thermal radiation across the gap. Radiative heat transfer was neglected because the local temperature difference between adjacent MH particles is very small compared to the absolute temperature. Natural convection (advection) was neglected for the same reason. The only remaining heat transfer mode to be considered was conduction.

An important simplifying assumption was that of local thermal equilibrium between the storage bed and hydrogen gas, meaning that the temperature in an infinitesimal layer at the solid–gas interface has a single value. Heat conduction occurs within the gas and within the particles, but not across the solid–gas interface, therefore. A corollary is that heat conduction in the solid and gas phases takes place in parallel so that there is no net heat transfer from one phase to the other. This makes it possible to represent the overall thermal resistance by two resistance chains in parallel.

The assumptions of no convection and local thermal equilibrium have been discussed at length by Nakagawa et al. [51] in the context of small laboratory-scale MH beds. They found that the effects of these assumptions were minor but discernible. The present model is concerned with real MH tanks at the kg H_2 scale, which generally have slower time response and so are likely in the authors' view to be consistent with these assumptions.

The reacted fraction defined by Eq. (3) refers only to the amount of hydrogen relative to the maximum possible amount and takes no account of the reality that most of the exchange of hydrogen between the solid and gas phases occurs during phase conversion. In reality the phase boundaries are not at 0 and $[H/M]_{max}$, but depending on the material are located a few percent above/below these values [48]. For this work this distinction was not taken into account because, in the authors' view, the added complexity of temperature-dependent phase boundaries was not necessary, given that perhaps 90% of the total hydrogen absorption/desorption takes place between the phase boundaries. This assumption slightly affects the accuracy of the expressions adopted for the volume expansion (details in § MH expansion) and all related parameters, and the enthalpy of phase conversion, which is taken to be a constant independent of F.

The thermal mass of the tank itself was neglected on the grounds that the temperature change within the flowing coolant should be small in a properly functioning MH tank, which was the case in the tank on which the new experiments reported here were conducted. This assumption is generally reasonable because (i) the metal-hydride temperature needs to be actively controlled by cooling during absorption and heating during desorption to maintain the operating pressure within design limits; (ii) the excursion in coolant temperature is much less than in the hydride bed; (iii) the mass of hydride should be much greater than the mass of the pressure vessel in a properly designed metal-hydride tank.

Mass and energy conservation

Let the hydrogen mass flow rate into the system be $\dot{\phi}$ per unit volume. For zero hydrogen flow, during absorption the local MH density ρ_s decreases, causing the local hydrogen gas density ρ_g to increase, and *vice versa* for desorption. The mass balance equations for the gas and solid are therefore.
for hydrogen

$$\varepsilon\frac{\partial\rho_g}{\partial t}+\frac{1}{r}\frac{\partial\left(r\rho_g v\right)}{\partial r}=\mp\,\dot{m}\pm\dot{\phi} \tag{4}$$

and

$$(1-\varepsilon)\frac{\partial\rho_s}{\partial t}=\pm\,\dot{m} \tag{5}$$

for the metal hydride, where the ' +' sign indicates absorption and the ' −' sign desorption. Here $\dot{m}$ is the mass source term of reaction per unit time and per unit volume, *i.e.* the hydrogen consumption during the hydrogenation, v is the superficial flow velocity of gas (details in § Gas velocity) and ε is the porosity (details in § Porosity). Assuming ideal gas behaviour, which is reasonable for the pressures typically encountered in MH tanks [17], the gas density is $\rho_g = PM_{H_2}/R_gT$.

The mass source term $\dot{m}$ can be written as [52].

$$\begin{aligned}&\text{Absorption:}\quad \dot{m}=(1-\varepsilon)(\rho_{sat}-\rho_s)\frac{dF}{dt}\\&\text{Desorption:}\quad \dot{m}=(1-\varepsilon)(\rho_s-\rho_{s,in})\frac{dF}{dt}\end{aligned} \tag{6}$$

where ρ_s is the density of the solid phase (metal or hydride), ρ_{sat} is the density of the solid phase when saturated with hydrogen, ρ_s , *in* is the density of the empty metal alloys and dF/dt is the rate of reaction (details in § Rate of reaction). Eq. (6) assumes that the density of the MH particles changes linearly with reacted fraction, *i.e.* obeys Vegard's Law on average.

Assuming local thermal equilibrium, $T_g = T = T_s$ and a single common energy balance equation can be written:

$$(\rho C_p)_{eff}\frac{\partial T}{\partial t}=\frac{1}{r}\frac{\partial}{\partial r}\left(k_{eff}r\frac{\partial T}{\partial r}\right)-\rho_g C_{pg}v\frac{\partial T}{\partial r}\pm\dot{m}\Delta H \tag{7}$$

here k_{eff} is the effective thermal conductivity of the MH bed (details in § Effective thermal conductivity), ΔH is the enthalpy of phase conversion, which is assumed to be constant, and $(\rho C_p)_{eff}$ is the effective thermal capacity of the MH bed, which can be expressed by a porosity-weighted function of the same quantities for the gas and MH as

$$(\rho C_p)_{eff}=\varepsilon(\rho C_p)_g+(1-\varepsilon)(\rho C_p)_s \tag{8}$$

Initial and boundary conditions

A proper set of boundary conditions must be defined to solve Eqs (4), (5) and (7). For the present scenario, the applicable boundary conditions are

Initials conditions:

$$P(r,0)=P_{in},\quad T(r,0)=T_{in} \tag{9}$$

Boundary conditions:

Cylindrical symmetry imposes an adiabatic boundary condition at $r = 0$:

$$\left.\frac{\partial T}{\partial r}\right|_{r=0}(0,t)=0 \tag{10}$$

At the external radius of the MH bed, $r = R$, continuity of the heat flux between the MH tank and the heat exchange fluid requires

$$-k_{eff}\left.\frac{\partial T}{\partial r}\right|_{r=R}(R,t) = h_f\left[T(R,t) - T_f\right] \tag{11}$$

where h_f is the convective heat transfer coefficient (details in § Heat transfer coefficient).

Properties of the MH bed

Specific heat

The specific heat of the MH increases relative to that of the empty metal with the absorption of hydrogen. Nakagawa et al. [51] developed the following semi-empirical expression for $LaNi_5$ which could be adjusted for other alloys:

$$(C_p)_s = \frac{6(3.1R + 10.04 \times [H/M]_{max}F)}{M_s + 6 \times [H/M]_{max}F} \times 1000 \tag{12}$$

here 3.1R is the assumed constant contribution to the molar specific heat from the metal and the contribution per added H mole of H is 10.04 J (mol. K)$^{-1}$. The factor 6 is appropriate for $LaNi_5H_6$. The factor 1000 occurs because the atomic weights are in gram.

MH expansion

Metals expand reversibly when absorbing hydrogen. Vegard's Law is well obeyed by many simple metal hydrides within the pure dilute and concentrated phases and is assumed here as an average over many MH particles in the full range of reacted fraction. If the relative expansion is τ_p (approx. 0.243 for $LaNi_5$), the density of the solid phase is then linearly related to the reacted fraction and can be expressed by Ref. [51].

$$\rho_s = p_{s,in}\frac{1 + F[w]_{max}}{1 + F\tau_p} \tag{13}$$

where $[w]_{max}$ is defined by Eq. (2).

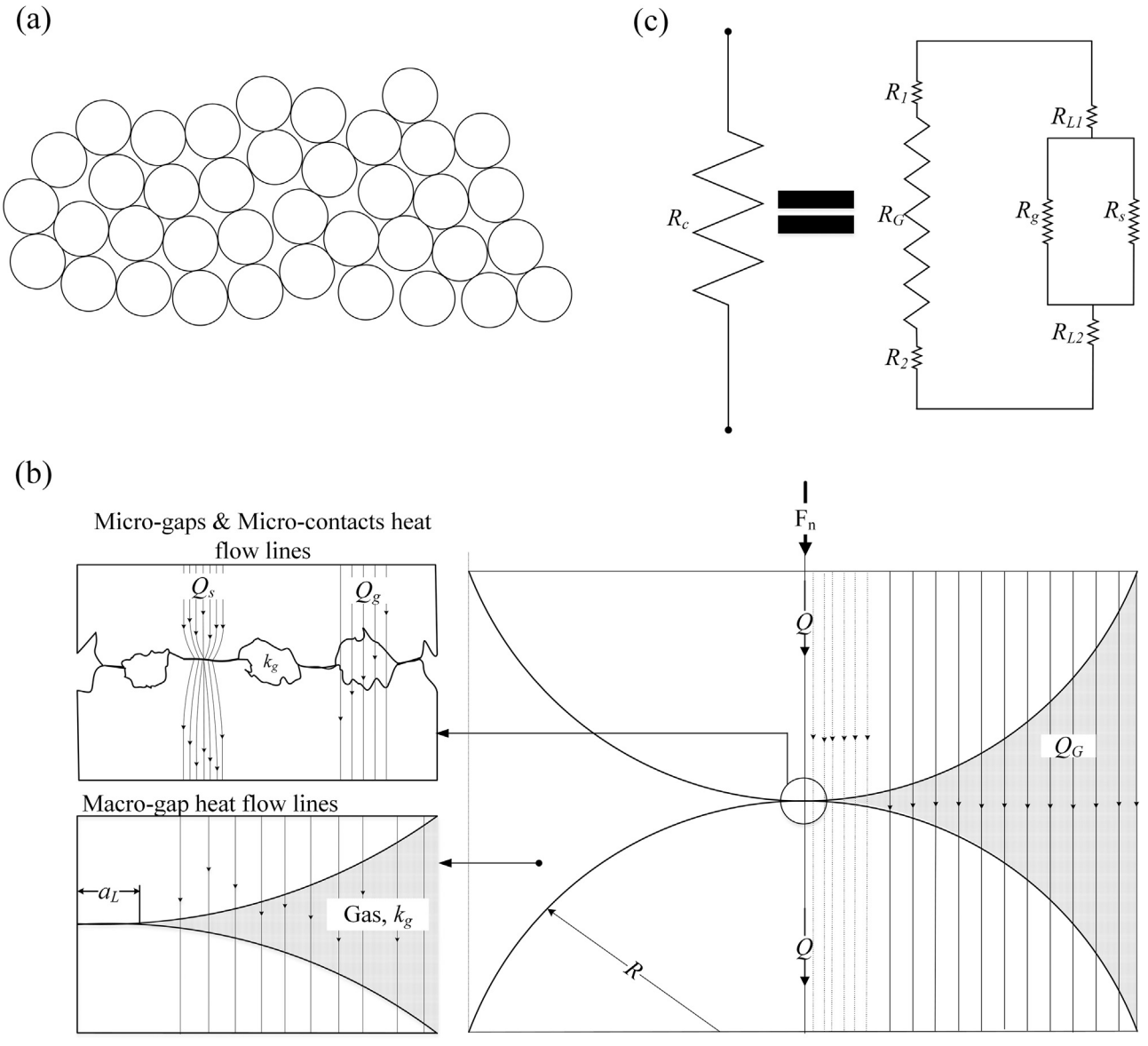

Fig. 1 – Model of thermal resistance between rough spheres [49], reproduced with permission. (a) Random structure of the MH bed; (b) Thermal contact between spheres in the presence of interstitial gas; (c) Equivalent thermal resistance network.

Effective thermal conductivity

For a uniform isotropic randomly packed assembly of perfect spheres with diameter D_p, Gusarov and Kovalev [50] obtained an exact expression for the effective thermal conductivity

$$k_{eff} = \frac{N(1-\varepsilon)}{\pi D_p R_c} \tag{14}$$

where N is the particle coordination number and R_c is the thermal contact resistance. The approach adopted here is based on this equation, with D_p taken to be the mean particle diameter of rough spheres and with a more realistic model of the actual contact between spheres. Expressions for the variables in Eq. (14) now need to be obtained in terms of the fundamental parameters introduced.

Assuming linear volume expansion,

$$D_p = D_{p,in}\left(1 + F\tau_p\right)^{1/3} \tag{15}$$

Van de Lagemaat et al. [53] found an empirical relationship between the effective coordination number of a random porous structure and its porosity as follows:

$$N = 3.08/\varepsilon - 1.13 \tag{16}$$

The remaining task preparatory to applying Eq. (14) is to calculate the thermal contact resistance between MH

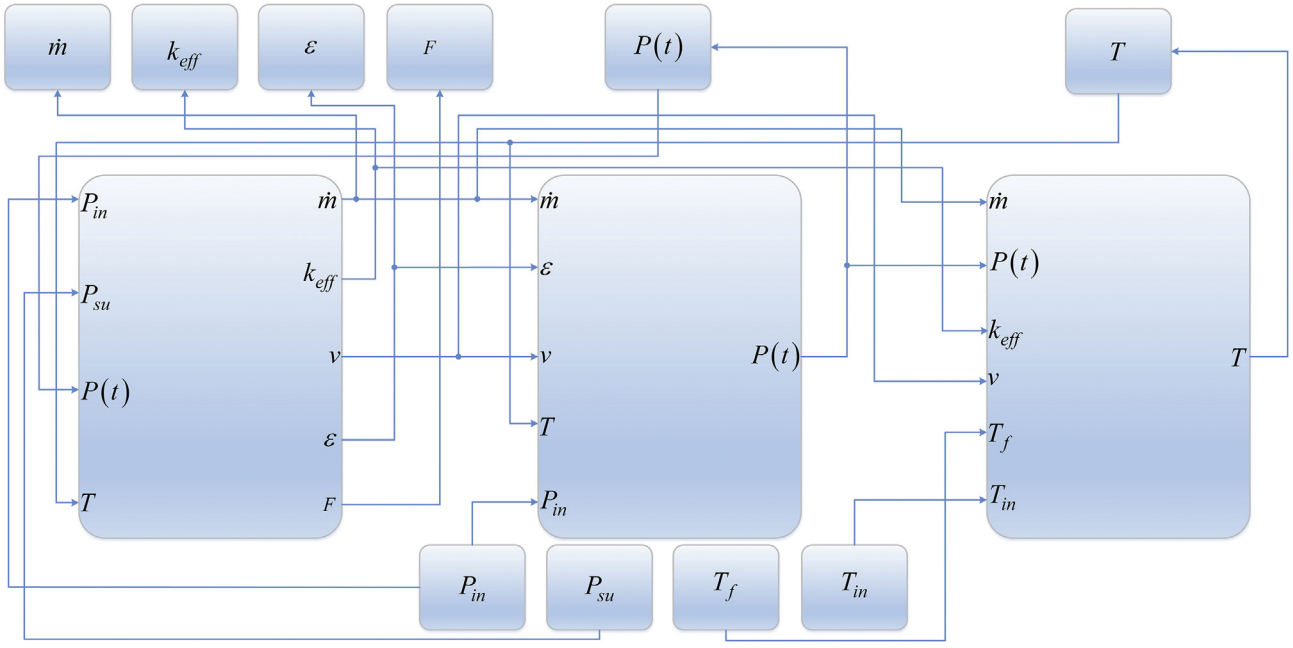

Fig. 2 – Simulink model of the MH tank.

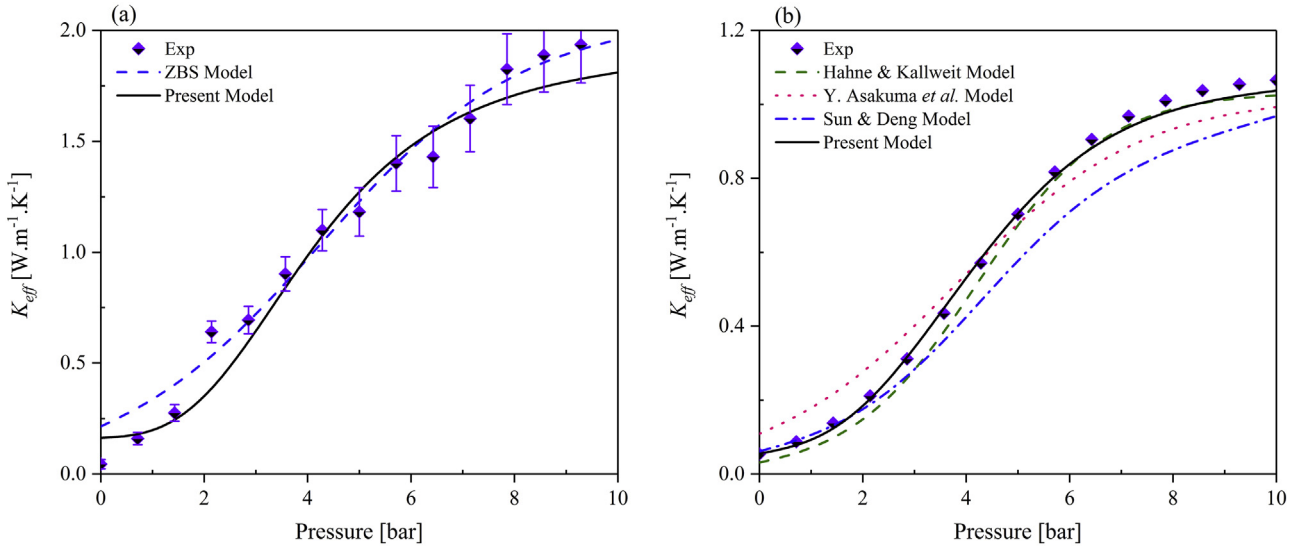

Fig. 3 – Comparison between the present and published models of the effective thermal conductivity. (a) $LaNi_5$–H_2 (b) $LaNi_{4.7}Al_{0.3}$–H_2.

particles. In reality the mechanical contact between particles is through micro-contacts at the apexes of surface asperities. The micro-contacts are distributed across the macro-contact area over which the particles notionally touch. Fig. 1 [49] depicts the adopted geometric and network models for the heat flow Q between isothermal planes through the two particles. The heat flow occurs *via* the gas in the macro-gap (effective resistance R_G) and the (mechanical) macro-contact

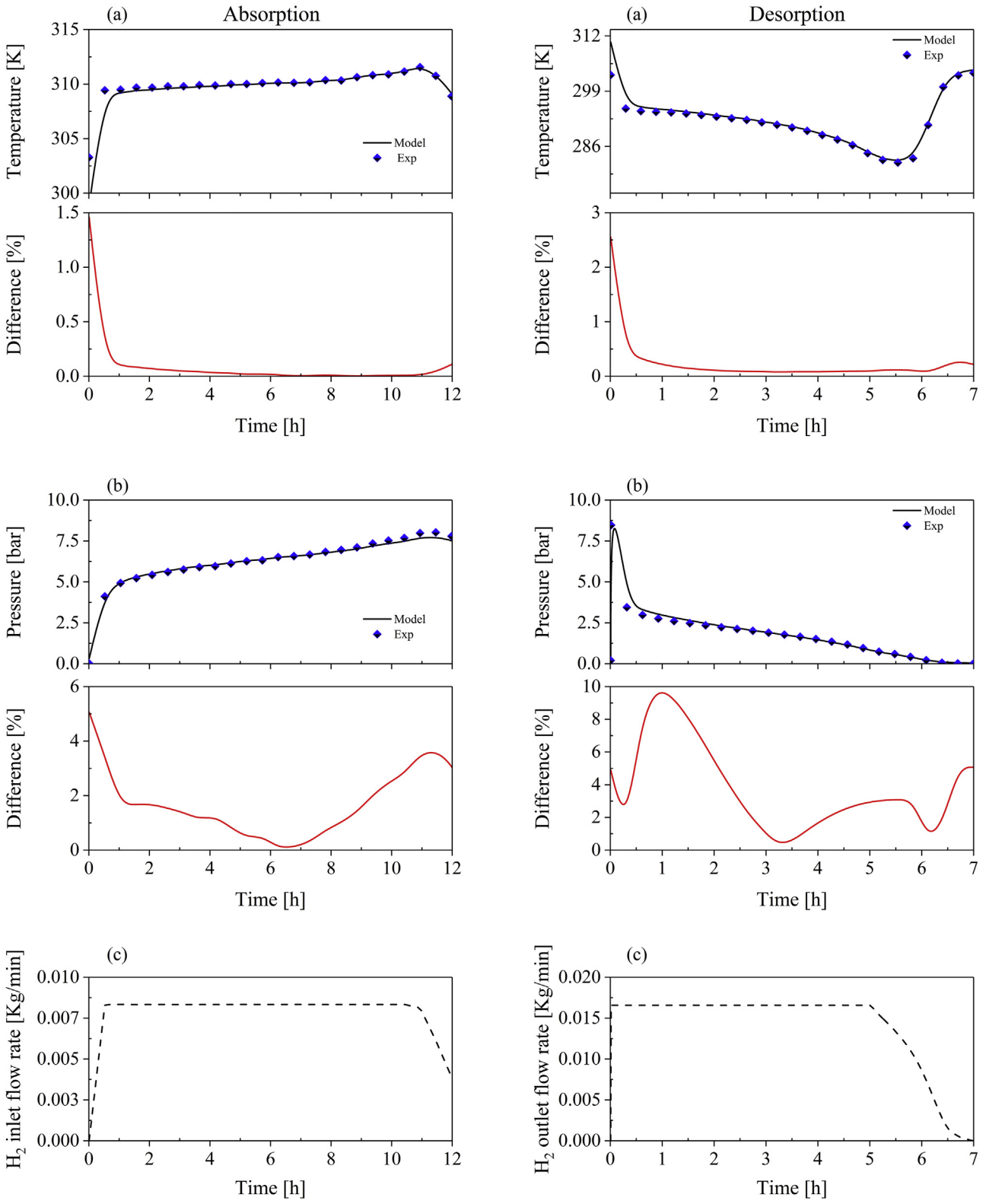

Fig. 4 – Comparison between experimental data (points) and model predictions (solid lines). (a) MH temperature 25 mm off tank axis; (b) hydrogen pressure at tank inlet; (c) hydrogen flow rate.

area, defined by the macro-contact radius, a_L. The resistance encountered on the latter path is that of the particles themselves assuming perfect contact (R_L) in series with micro-contacts (effective additional resistance R_s) in parallel with micro-gaps containing interstitial gas (effective additional resistance R_g).

Conduction via the macro-gap and the contact area occurs in parallel, so the thermal contact resistance is given by

$$\frac{1}{R_c} = \left[\frac{1}{R_{mic} + R_L} + \frac{1}{R_G}\right] \tag{17}$$

where $R_{mic} = [R_s R_g / (R_s + R_g)]$ and R_G has three components: the macro-gap resistance of the gas and R_1 and R_2, corresponding to the bulk thermal resistances of the solid portions of the path through the two spheres. The bulk resistances R_1 and R_2 are considered negligible compared to R_G because the thermal conductivity of the gas is much smaller than that of the solid (*i.e.* $k_g << k_s$).

The thermal resistance of a macro-contact with radius a_L is [59].

$$R_L = \frac{1}{2k_s a_L} \tag{18}$$

Assuming plastically deformed asperities, Bahrami et al. [54] developed a compact model for the thermal resistance of a micro-contact follows:

$$R_s = \frac{0.565 H_v d_v}{k_s F_n} \tag{19}$$

where F_n is the normal contact force, H_v is the Vickers microhardness and d_v is the mean indentation diagonal depth (the depth from the surface of the sample to the indenter tip). H_v can be calculated as follows [55].

$$H_v = c_1 (d_v)^{c_2} \tag{20}$$

where c_1 and c_2 are the Vickers microhardness coefficients. The normal contact force F_n can be calculated by

$$F_n = \frac{4}{3} E' R^{1/2} d_v^{1.5} \tag{21}$$

where $R = D_p/2$ is the sphere radius, E' is the effective elastic modulus, which can be estimated from Fig. 4 of Ref. [56]. The radius of macro-contact can be calculated by Ref. [57].

$$\frac{a_L}{a_H} = \begin{cases} 1.605/\sqrt{\varepsilon} & \text{if } 0.01 \le \varepsilon \le 0.47 \\ 3.51 - 2.51\varepsilon & \text{if } 0.47 \le \varepsilon \le 1 \end{cases} \tag{22}$$

where the Hertzian contact radius, a_H, is given by Ref. [57].

$$a_H = (0.75 F_n R / E')^{1/3} \tag{23}$$

Bahrami et al. [58] developed a model for heat conduction through the interstitial gas between rough spherical bodies. The thermal resistances of the interstitial gas in the micro-gap and the macro-gap were calculated by integrating these surface elements over the macro-contact and the macro-gap areas, respectively. The micro-gap resistance for the contact of two rough spheres was obtained as

$$R_g = \frac{\sqrt{2}\sigma a_2}{\pi k_g a_L^2 \ln\left[1 + a_2 \Big/ \left(a_1 + M/\sqrt{2}\sigma\right)\right]} \tag{24}$$

where σ is the surface roughness, M is the gas parameter (defined below) and

$$\begin{aligned} a_1 &= erfc^{-1}(2P_{max}/H_c) \\ a_2 &= erfc^{-1}(0.03P_{max}/H_c) - a_1 \end{aligned} \tag{25}$$

where P_{max} is the maximum contact load pressure,

$$P_{max} = \frac{2}{\pi} E' (d_v/R)^{0.5} \tag{26}$$

and H_c is the contact microhardness, given by

$$H_c = c_1 (1.62 d_v)^{c_2} \tag{27}$$

The gas parameter, M, is given by Ref. [55]

$$M = \left(\frac{2 - \alpha_{T_1}}{\alpha_{T_1}} + \frac{2 - \alpha_{T_2}}{\alpha_{T_2}}\right)\left(\frac{2\gamma}{1+\gamma}\right)\frac{1}{Pr} l_m \tag{28}$$

where α_T is the thermal accommodation coefficient, γ is the ratio of gas specific heats (adiabatic exponent, 1.4 for hydrogen), Pr is the gas Prandtl number (0.6 for hydrogen) and l_m is the molecular mean-free path. The thermal accommodation coefficients α_{T1} & α_{T2} depend on the gas–solid combination. Usually, these parameters have second-order effects and slight variations in their values will not have a significant impact on the effective thermal conductivity [49].

At low pressures the thermal conductivity of a gas decreases because of the increase in the mean free path compared to the size of the container. The thermal conductivity of hydrogen is given by Ref. [59]

$$k_g = \frac{k_{ref}}{1 + 2b \times Kn} \tag{29}$$

where k_{ref} is the thermal conductivity of the gas at reference pressure (1 bar), b is a dimensionless constant specific to the gas (9.87 for hydrogen) and

$$Kn = \frac{l_m}{D_p} \tag{30}$$

is the Knudsen number. The mean free path as a function of gas pressure P is calculated as follows [59]:

$$l_m = \frac{6(\gamma - 1)}{(9\gamma - 5)} \times \frac{k_g}{P}\left(\frac{M_{H_2} T}{2k_B}\right)^{1/2} \tag{31}$$

The macro-gap resistance for the contact of two rough spheres can be calculated as follows [50]:

$$R_G = \frac{1}{2\pi k_g D_p \left[\frac{1}{2}\ln(1+L) + \ln\left(1+\sqrt{L}\right) + \frac{1}{1+\sqrt{L}} - 1\right]} \tag{32}$$

where

$$L = \frac{\gamma + 1}{9\gamma - 5} \times \frac{3}{4Kn\sqrt{\pi}} \tag{33}$$

Rate of reaction

As mentioned, the apparent kinetics of hydrogen absorption/desorption by a MH bed is dominated by heat flow. The reason is that the intrinsic kinetics of the MH is typically fast compared to the real rate of change of the global hydrogen concentration, unless the MH is thermally clamped. This

means that the MH is essentially in equilibrium with its surroundings at the local temperature and pressure. The details of the intrinsic strictly isothermal reaction kinetics therefore affect the MH tank response relatively little, and a generic kinetics model is likely to be satisfactory. Supposing that the reaction is controlled by diffusion or the phase transformation, we may assume that the reaction is first-order or nearly so and therefore expect exponential time response. The other factors to be included are temperature dependence of the rate and the pressure drive, meaning the effect of the difference between the local hydrogen pressure and the equilibrium pressure corresponding to the local hydrogen concentration.

For absorption, with rate constant k_a

$$F = 1 - \exp(-k_a t) \tag{34}$$

and the reaction rate is

$$\frac{dF}{dt} = k_a(1 - F) \tag{35}$$

The pressure and temperature dependencies can be included in k_a as follows [14,38,42]:

$$k_a = \frac{\kappa_a}{(1-\varepsilon)} \exp\left(-\frac{E_a}{R_g T}\right) \ln\left(\frac{P}{P^a_{eq}}\right) \tag{36}$$

where κ_a is a material-dependent intrinsic absorption rate constant, E_a is a notional absorption activation energy capturing the temperature dependence of the rate, and P^a_{eq} is the equilibrium absorption pressure (details in § Equilibrium pressure).

For desorption, with rate constant k_d

The reacted fraction for desorption can be expressed as follows

$$F = \exp(-k_d t) \tag{37}$$

and the reaction rate is

$$\frac{dF}{dt} = -k_d F \tag{38}$$

The rate constant is

$$k_d = \frac{\kappa_d}{(1-\varepsilon)} \exp\left(-\frac{E_d}{RT}\right)\left(\frac{P^d_{eq} - P}{P^d_{eq}}\right) \tag{39}$$

where κ_d is a material-dependent intrinsic desorption rate constant, E_d is a notional desorption activation energy and P^d_{eq} is the equilibrium desorption pressure.

Porosity

The average porosity of the MH bed is defined as

$$\varepsilon = 1 - \frac{V_s}{V_T} \tag{40}$$

where V_s is the total volume of solid particles and V_T is the total volume of the bed including particles and pores. The porosity varies owing to expansion of the individual MH particles during absorption and contraction during desorption by the relative factor τ_p defined in association with Eq. (13). The overall relative change in the total pore volume is not in general $1 - \tau_p$, however, because of compaction caused by the increased mechanical pressure between the expanding particles, which offsets the increase in packing fraction. Matsushita et al. [60] calculated the resulting porosity relative to that of the empty MH bed, ε_0, as follows:

Absorption:

$$\varepsilon_a = 1 - (1 - \varepsilon_0)\left[\frac{1 + \tau_p F}{1 + \tau_a F}\right] \tag{41}$$

Desorption:

$$\varepsilon_d = \begin{cases} 1 - (1-\varepsilon_0)\left[\dfrac{1+\tau_p F}{1 + \tau_a F_{max} - \left(1 - \dfrac{\tau_p}{\tau_a} F\right)\tau_d}\right] & \text{if } 0 < F < \dfrac{\tau_a}{\tau_p} \\ 1 - (1-\varepsilon_0)\left[\dfrac{1+\tau_p F}{1+\tau_a F_{max}}\right] & \text{if } \dfrac{\tau_a}{\tau_p} < F < 1 \end{cases} \tag{42}$$

where τ_a is the packed bed expansion ratio during absorption.

Gas velocity

For flow in the radial direction only, the superficial flow velocity, v, of the gas within the MH bed can be described by Darcy's law in the following form:

$$v = -\frac{K_p}{\mu}\frac{\partial P}{\partial r} \tag{43}$$

where K_p is the permeability of MH bed and μ is the kinematic viscosity of the gas, taken to be constant in the relevant range of conditions. The permeability may be calculated using the Blake–Kozenye semi-empirical expression describing the laminar flow of a Newtonian fluid through a packed bed which is long and wide compared to the particle size [61]:

$$K_p = \frac{D_p^2 \varepsilon^3}{150(1-\varepsilon)^2} \tag{44}$$

The factor of 150 appearing in the denominator has been established experimentally [62]. The mean particle diameter may be obtained by direct measurement or in terms of a sphere-equivalent relationship to the experimentally determined total surface area via the parameter a_v, defined as the ratio of the total particle surface area to the total volume of particles in the bed:

$$D_p = 6/a_v \tag{45}$$

Eq. (43) then becomes

$$v = -\frac{D_p^2 \varepsilon^3}{150\mu(1-\varepsilon)^2}\frac{\partial P}{\partial r} \tag{46}$$

Equilibrium pressure

The equilibrium (in the sense of quasi-static) absorption–desorption behaviour of a metal hydride is generally captured by measuring pressure–composition isotherms in a range of temperatures. Absorption occurs when the local hydrogen pressure exceeds the equilibrium pressure, P_{eq}, at the local temperature and *vice-versa* for desorption. Very many equations have been proposed. The equation adopted here was developed by Mohammadshahi et al. [17] for $LaNi_5$–H_2, based on new experiments:

Table 2 – Fixed parameters for $LaNi_5$-H_2 system.

Parameters	Value	Ref.
ΔH_a / ΔH_d	30 kJ mol^{-1}	[17]
κ_a	59.187 s^{-1}	[73]
κ_d	9.57 s^{-1}	[73]
E_a	20.57 kJ mol^{-1}	[31]
E_d	16.71 kJ mol^{-1}	[73]
$k_{g,ref}$	0.167 W m^{-1} K^{-1}	[31]
k_s	2.0 W m^{-1} K^{-1}	[31]
ε_0	0.5	[17]
ρ_{sat}	8527 kkg m^{-3}	[13]
ρ_{in}	8400 kkg m^{-3}	[13]
C_{p_g}	14.95 kJmol^{-1}K^{-1}	[31]
$C_{p_{s,in}}$	0.419 kJmol^{-1}K^{-1}	[31]
μ_g	1.03 × 10^{-4} m^2 s^{-1}	[31]
D_{in}	12 μm	–
τ_a	0.177	[73]
τ_d	0.0816	[73]
τ_p	0.246	[73]
w	1.4%	[73]
σ	0.12 μm	[58]
c_1 /c_2	7.3 GPa/−0.27	[58]
α_{T_1} /α_{T_2}	0.69/0.83	[17]
b	9.87	[59]
γ	1.4	[50]

Table 3 – Fitted parameters.

Parameters	Value
Re_a	1920
Re_d	2875
Pr_a	59
Pr_d	97
d_v	29.37 μm ($LaNi_5$), 31.11 μm ($LaNi_{4.7}Al_{0.3}$)

$$P_{eq} = \left[\frac{C_0 C_1 F^{C_2}}{1 + C_1 F^{C_2}} + C_3 F + e^{C_4(F - C_5)}\right] \exp\left[-K\left(\frac{1}{T} - \frac{1}{T_{ref}}\right)\right] \quad (47)$$

where C_0 –C_5 and K are fitted coefficients. The ideal value of K is ΔH /R. The exponential builds-in the fact that most metal hydrides obey Arrhenius' Law. The leading terms account for the existence of a sloped plateau. If the MH exhibits pressure hysteresis, the values of C_0 –C_5 are different for absorption and desorption cycles. The values for $LaNi_5$ can be found in Ref. [17].

Heat transfer coefficient

In the case of forced convection of the circulating coolant through the heat exchanger, the average heat transfer coefficient for longitudinal flow over a cylinder can be found from the average Nusselt number as follows

$$h_f = \frac{\overline{Nu} k_f}{D_{tn}} \quad (48)$$

where D_{tn} is the diameter of the tank and k_f is the thermal conductivity of the fluid. The average Nusselt number can be found from the following empirical relation presented by Bergman et al. [63] as follows

$$\overline{Nu} = 0.3 + \frac{0.62 Re^{1/2} Pr^{1/3}}{\left[1 + (0.4/Pr)^{2/3}\right]^{1/4}} \left[1 + \left(\frac{Re}{282000}\right)^{5/8}\right]^{4/5} \quad (49)$$

where Re is the Reynolds number and Pr is the Prandtl number.

Numerical procedure

The governing equations were solved in Simulink and Matlab. The method of characteristics was used for solving the mass balance equations (Eqs (4) and (5)), which can be expressed in the following general form

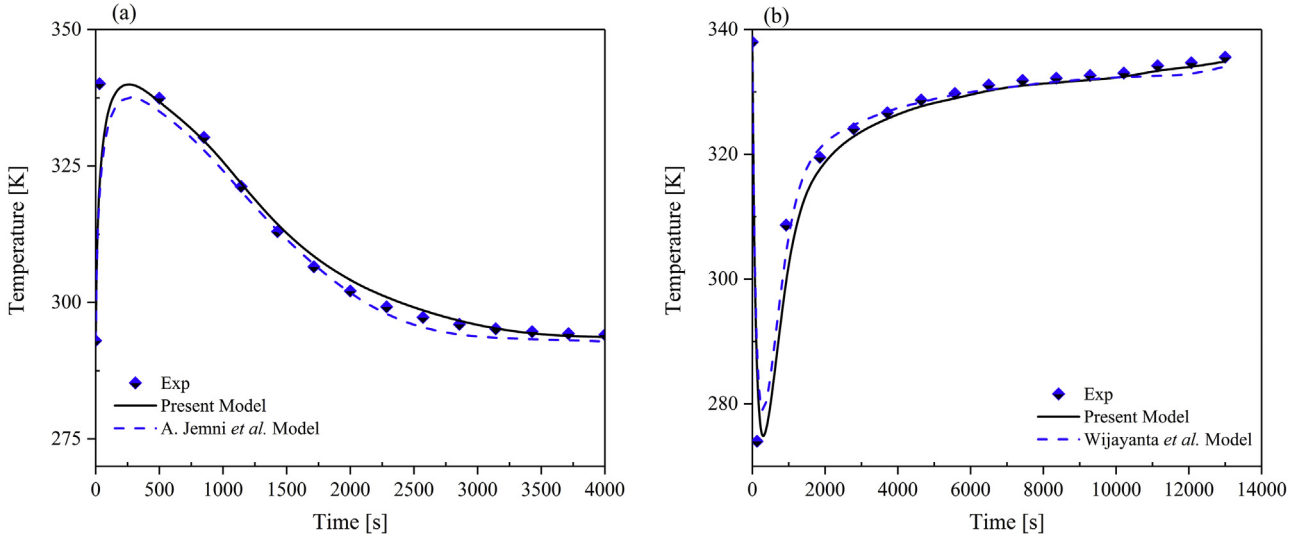

Fig. 5 – Comparison between present and published model to experimental data (a) absorption (b) desorption.

$$\frac{d}{ds}u(r(s),t(s)) = f(u,r(s),t(s)) \tag{50}$$

The energy conservation equation (Eq. (7)) was solved by combining separation of variables and superposition. Eq. (7) is a nonhomogeneous partial differential equation (PDE) and it has nonhomogeneous boundary condition as well. First, the nonhomogeneous boundary condition was treated by shifting the temperature to $\Theta\ (r\ ,t\ ) = T\ (R\ ,t\ ) - T_f$, which yields the following general form of Eq. (7):

$$\frac{\partial\Theta(r,t)}{\partial t} = X\frac{\partial^2\Theta}{\partial r^2} \pm \dot{m}\Delta H \times \exp\left\{-\left[\frac{\Gamma}{2X}r - \frac{\Gamma^2}{4X}t\right]\right\} \tag{51}$$

Initial condition:

$$\Theta(r,0) = T_{in} \tag{52}$$

Boundary condition:

$$\left.\frac{\partial\Theta}{\partial r}\right|_{r=0}(0,t) = 0 \tag{53}$$

$$-k_{eff}\left.\frac{\partial\Theta}{\partial r}\right|_{r=R}(R,t) = h_f\Theta|_{r=R} \tag{54}$$

Here X is the exchange coefficient and Γ is a function of $\rho_g C_{pg}\vec{v}$. Hence the solution of Eq.(51) can be characterised using superposition as follows

$$\Theta(r,t) = \Psi(r,t) + \Phi(r) \tag{55}$$

where $\Psi\ (r\ ,t\ )$ is a solution of the homogenous form of the PDE and $\Phi\ (r\ )$ is a solution of the steady-state problem with generation/source term.

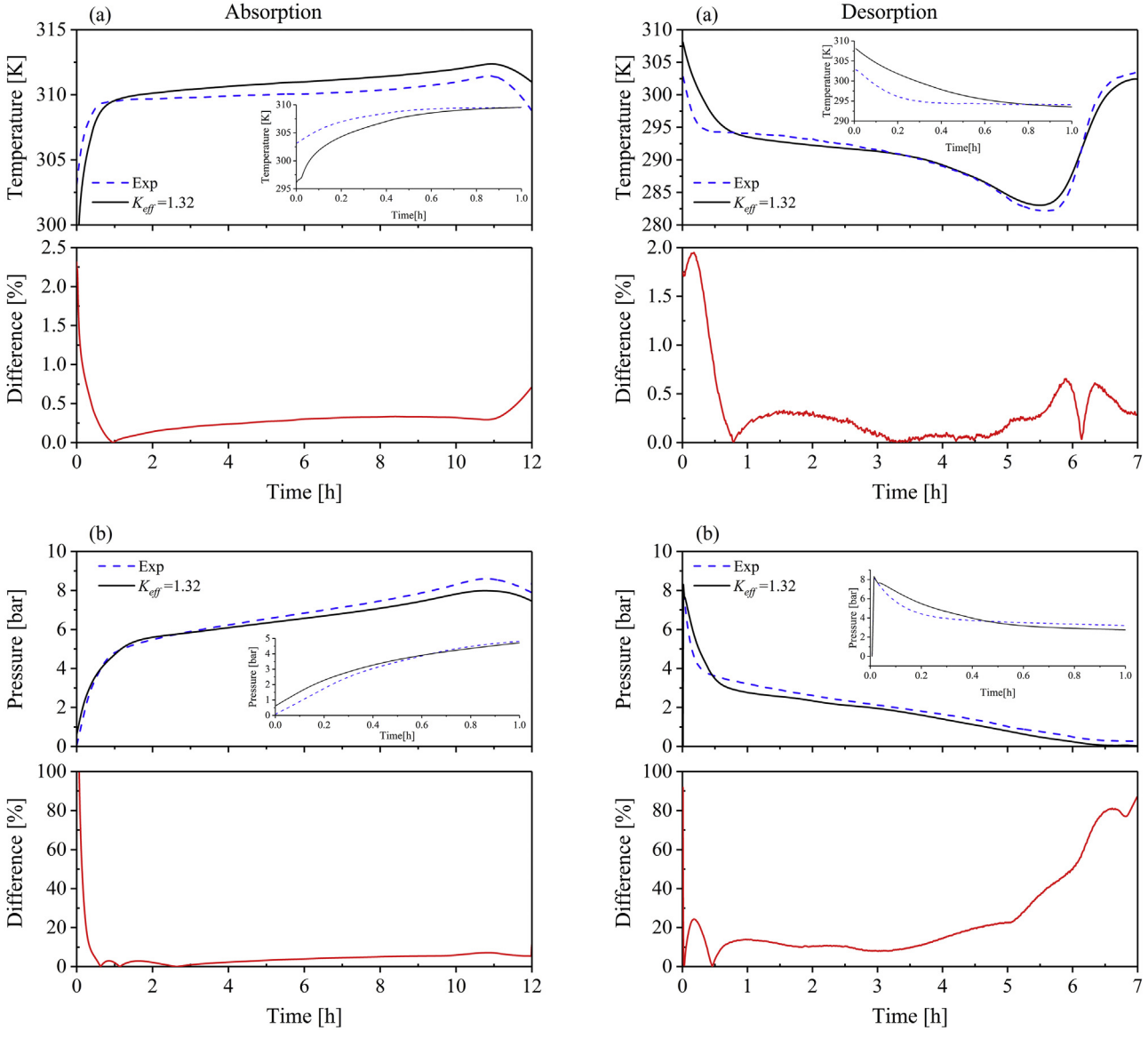

Fig. 6 – Comparison between experimental data and model prediction with constant effective thermal conductivity, $K_{eff} = 1.32\ W\ m^{-1}\ K^{-1}$. (a) MH temperature 25 mm off tank axis; (b) hydrogen pressure at tank inlet.

Result and discussions

Fig. 2 depicts the full Simulink model of the MH tank, shows how the parameters discussed in the previous section contribute to the simulation and maps the interactions between them.

Effective thermal conductivity

The new effective thermal conductivity model was tested using experimental data reported in Ref. [64] for the $LaNi_5$–H_2 system, and also compared to one published model [65] as shown in Fig. 3a, by adopting the parameters from Ref. [64], without fitting. The prediction of the new model is at least as good as the published model.

Fig. 3b compares the new effective thermal conductivity model and three published models [66,69,70] to experimental data for the $LaNi_{4.7}Al_{0.3}$–H_2 system, adopting parameters from the Ref. [66]. The new model Provides an improved fit.

Absorption/desorption kinetics

New experiments

The new tank model was tested against experimental data for absorption and desorption by a MH storage module containing two identical cylindrical tanks with internal diameter approximately 200 mm and a total capacity of 6.4 kg H_2, as installed in the off-grid energy system of the Sir Samuel Griffith Centre at Griffith University [3]. The hydrogen storage alloy is a multi-component AB_5 analogue proprietary to Japan Steel Works for which equilibrium pressure–composition isotherms were available. These were fitted using Eq. (47). Values for most physical parameters were adopted from the literature for $LaNi_5$.

Following an initial evacuation, hydrogen was supplied via a flow controller at 0.094 $Nm^3\ min^{-1}$ (0.52 kg h^{-1}) during absorption and withdrawn at 0.187 $Nm^3\ min^{-1}$ (1.03 kg h^{-1}) during desorption. The outer heat exchanger jacket was connected to a thermostatic water reservoir with approx. 1 m^3 capacity to stabilise the inlet temperature to the heat exchanger, which was 30.4 °C during absorption and 30.2 °C during desorption. The MH temperature was sampled by a thermocouple located 25 mm off the tank axis with an insertion depth of 200 mm.

Fig. 4 compares the measured and fitted MH bed temperature and hydrogen pressure at the tank inlet. The new model clearly fitted the experimental data very well, except for the initial transients.

Table 2 lists the values adopted from literature for the fixed parameters. Parameters that could not be reliably estimated, mostly because they are difficult to measure directly, were obtained by fitting the model to experimental data. These include the Reynolds number (*Re*), Prandtl number (*Pr*), and the mean indentation diagonal depth (d_v). The fitted parameter values are listed in Table 3 and compared to published values below.

The fitted values for Reynolds number and Prandtl number lie within the expected ranges found in the literature for heat transfer by forced convection over a cylinder: $2 \times 10^3 < Re < 10^5$ and $0.7 < Pr < 176$ [67]; $1.0 < Re < 1 \times 10^5$ and $0.67 < Pr < 300$ [68].

Mordovin et al. [71] and Joubert et al. [72] measured mean indentation diagonal depth values for $LaNi_5$ and $LaNi_{4.7}Al_{0.3}$ alloys between 29 and 33 μm. The fitted values lie within this range.

Comparison to published models

The new tank model was also tested against two published models. Askri et al. [74] developed a two-dimensional mathematical model for absorption and validated it against experimental data published by Jemni et al. [35]. The control volume finite element method (CVFEM) was used to solve the governing equations of their model. Wijayanta et al. [42] carried out an experiment and developed a two-dimensional mathematical model for absorption and desorption. They

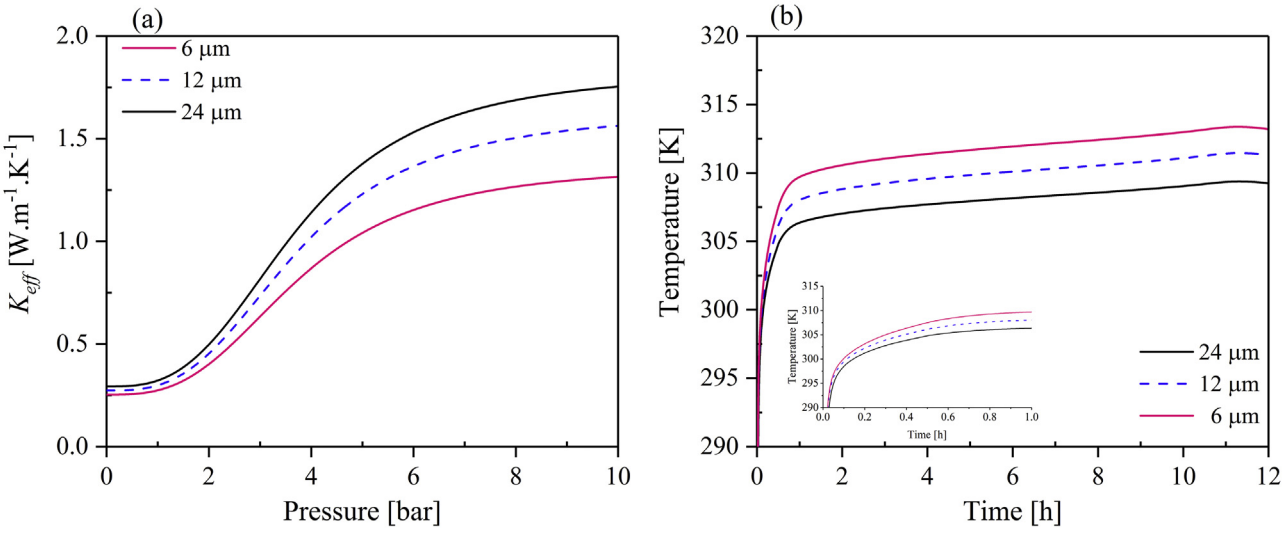

Fig. 7 – Effect of particle size during absorption. (a) Effective thermal conductivity; (b) MH temperature 25 mm off tank axis.

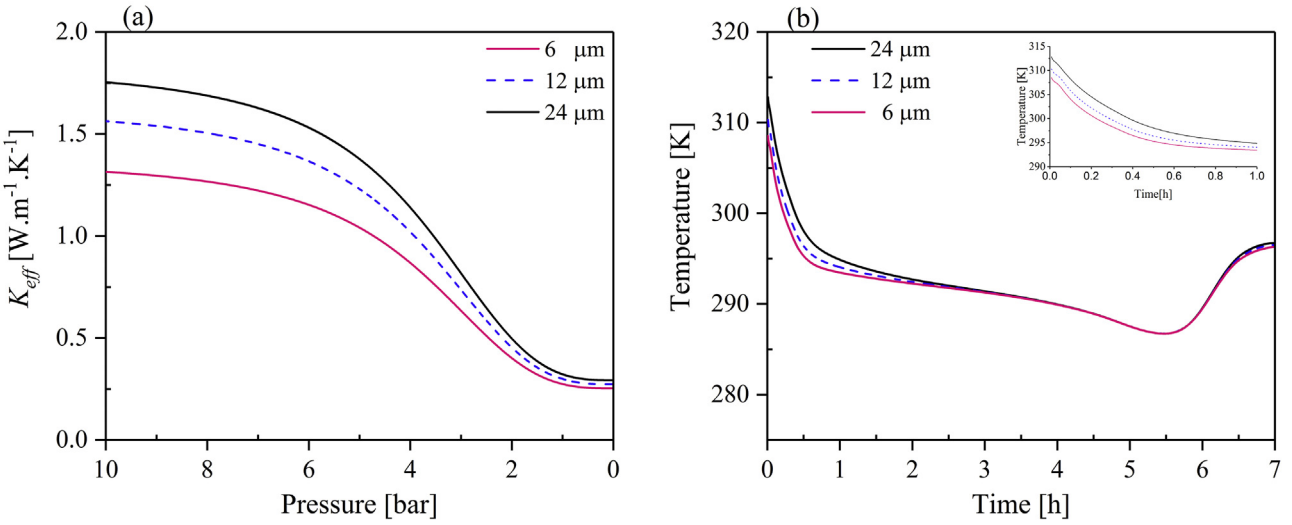

Fig. 8 – Effect of particle size during desorption. (a) Effective thermal conductivity; (b) MH temperature 25 mm off tank axis.

also solved the governing equations using the CVFEM. Fig. 5 compares the new model and published models to experimental data for absorption and desorption, made by adopting the model parameters from the particular published models [42,74]. The new one-dimensional model is at least as accurate as the published two-dimensional models.

Model exploration

Fig. 6 compares the model fit to the same experimental data as in Fig. 4, but with the ETC held constant at 1.32 W m^{-1} K^{-1}. The fit is significantly worse, demonstrating the improvement owing to the more detailed ETC model.

Figs. 7 and 8 explore the effects of average particle size on tank performance via the temperature near the tank axis. The model parameters were the same as those used to model the experimental data in Fig. 4, except that the particle size was varied. Referring to Fig. 4, during absorption the pressure reached 5 bar within the first hour, by which pressure the ETC has nearly saturated (Fig. 7a). After this time, the effect on temperature (Fig. 7b) is consequently a roughly constant increase with decreasing particle size. During desorption (Fig. 8), the relatively minor effect of particle size in temperature relates to the rapid fall in pressure to the point (about 2 bar) where the ETC changes little.

Discussion

Generally speaking the new model predicts the measured values of temperature (Figs. 5 and 6) very well, except for the transients occurring when absorption by the empty tank and desorption by the full tank are initiated. Noting that assuming a constant ETC value (1.32 W m^{-1} K^{-1}; Fig. 6a) which is much higher than the likely value at low pressure does not greatly affect the initial temperature transient behaviour in absorption, the simplified kinetic model is the likely cause. Because absorption in the α phase and desorption in the β phase do not require nucleation of the other phase, the kinetics speeds up in each case. This means that the α/α+β or β/β+α phase boundary is reached sooner, causing earlier enthalpy release/absorption and a faster than expected temperature excursion. The presented model could be modified to take account of the differences between the pure and transforming phases if following transient behaviour were important.

Pressure hysteresis is a potentially important characteristic behaviour of real metal hydrides that should be taken into account for MH tanks that are cycled within the two-phase region, by, for instance, being driven into desorption before being completely filled with hydrogen. The experimental data modelled here (Fig. 4) were taken during absorption/desorption from the empty/full states. Pressure hysteresis is accounted for in the model only indirectly, through the two sets of parameters associated with Eq. (47). A full accounting requires that the direction of concentration change be taken into account at every position in the MH bed, which requires a finite-element approach. The different thermal and kinetic parameters of the pure and transforming phases also need be taken into account. This point is discussed further by Mohammadshahi et al. [20]. The data in Fig. 4 are for an alloy that exhibits very little hysteresis, which is very desirable in a real MH tank since hysteresis represents cyclic energy loss.

The comparison with experimental data was carried out for MH tanks with cylindrical symmetry, no axial variation and an outer heat exchanger. The model works very well for such tanks, but a question worth asking is whether the same model could be applied to a more complex tank with acceptable fidelity. Incorporation of a high-conductivity material (mesh, foam or powder) would be straightforward by modifying the thermal resistance model with an additional term in parallel with the gap resistance. The other major tank type, that with an axial coolant tube carrying many radial fins, could probably be approached with a 1D model by neglecting radial heat flow.

Summary and conclusions

The objective of the work was to develop a MH tank model that would be tractable in a simulation environment, in which finite-element analysis in multiple dimensions is unwieldy. A one-dimensional model was developed for a MH tank for hydrogen storage, based on linked modular mathematical models in Simulink®. Finite-element analysis was not used. Because the apparent kinetics of a practicable MH tank is dominated by heat flow originating in the enthalpy of hydrogen absorption/desorption, particular attention was paid to modelling the effective thermal conductivity, based on a detailed description of the thermal resistance between touching hydride particles.

The thermal conductivity model was tested against published experimental data and published CVFEM 2D models, for $LaNi_5$ and $LaNi_{4.7}Al_{0.3}$. The 1D model performed at least as well as the published models.

The MH tank model was first tested against our own experimental data for a pair of hydrogen storage tanks with 6.4 kg total hydrogen capacity, and then compared with a published 2D model and published experimental data. The new model performed very well, except during transients in the hydrogen flow, probably owing to the first-order model of MH kinetics used. Comparing the results of modelling with constant and pressure-dependent effective thermal conductivity, the fidelity of the tank model was much better with the more realistic ETC model.

As an example of the advantage of a physically-based model, the effect of changing the average particle size could be predicted and led to significant changes in the predicted MH bed temperature.

Thus the approach of using a simplified 1D model based on a physical model of effective thermal conductivity has been demonstrated to be tractable and accurate without resort to finite-element methods, at least for tanks with cylindrical symmetry and no axial variation. This also demonstrates that a wholly empirical approach, while convenient, is largely unnecessary. Further exploration of this approach for tanks with more complicated internals, such as heat-conducting foam or radial fins, is warranted.

Acknowledgements

ZA acknowledges receipt of a postgraduate scholarship from Griffith University. The authors thank H. Itoh for the experimental data shown in Fig. 4 and T.J. Gould for advice on solving the governing equations.

REFERENCES

[1] Schlapbach L, Züttel A. Hydrogen-storage materials for mobile applications. Nature 2001;414(6861):353–8.
[2] Reilly JJ, Adzic GD, Johnson JR, Vogt T, Mukerjee S, McBreen J. The correlation between composition and electrochemical properties of metal hydride electrodes. J Alloy Comp 1999;293:569–82.
[3] Sir Samuel Griffith Centre, Griffith University, Brisbane, Auatralia. Accessed via: www.griffith.edu.au.
[4] Henn-na Hotel, Nagasaki, Japan. Accessed via: www.h-n-h.jp/en/concept/.
[5] Gray EMacA, Webb CJ, Andrews J, Shabani B, Tsai PJ, Chan SLI. Hydrogen storage for off-grid power supply. Int J Hydrogen Energy 2011;36(1):654–63.
[6] Buschow KH, Van Mal HH. Phase relations and hydrogen absorption in the lanthanum-nickel system. J Less Common Met 1972;29(2):203–10.
[7] Askri F, Jemni A, Nasrallah SB. Prediction of transient heat and mass transfer in a closed metal–hydrogen reactor. Int J Hydrogen Energy 2004;29(2):195–208.
[8] Ron M, Gruen D, Mendelsohn M, Sheet I. Preparation and properties of porous metal hydride compacts. J Less Common Met 1980;74(2):445–8.
[9] Goodell PD, Rudman PS. Hydriding and dehydriding rates of the $LaNi_5$-H system. J Less Common Met 1983;89(1):117–25.
[10] Abdin Z, Webb CJ, Gray EMacA. Modelling and simulation of a proton exchange membrane (PEM) electrolyser cell. Int J Hydrogen Energy 2015;40(39):13243–57.
[11] Abdin Z, Webb CJ, Gray EMacA. PEM fuel cell model and simulation in Matlab–Simulink based on physical parameters. Energy 2016;116:1131–44.
[12] Abdin Z, Webb CJ, Gray E MacA. Modelling and simulation of an alkaline electrolyser cell. Energy 2017;138:316–31.
[13] MacDonald Brendan D, Rowe Andrew M. Impacts of external heat transfer enhancements on metal hydride storage tanks. Int J Hydrogen Energy 2006;31(12):1721–31.
[14] Nyamsi SN, Yang F, Zhang Z. An optimization study on the finned tube heat exchanger used in hydride hydrogen storage system–analytical method and numerical simulation. Int J Hydrogen Energy 2012;37(21):16078–92.
[15] Mohammadshahi SS, Gray E MacA, Webb CJ. A review of mathematical modelling of metal-hydride systems for hydrogen storage applications. Int J Hydrogen Energy 2016;41(5):3470–84.
[16] Mellouli S, Khedher NB, Askri F, Jemni A, Nasrallah SB. Numerical analysis of metal hydride tank with phase change material. Appl Therm Eng 2015;90:674–82.
[17] Mohammadshahi SS, Gould T, Gray E MacA, Webb CJ. An improved model for metal-hydrogen storage tanks–part 1: model development. Int J Hydrogen Energy 2016;41(5):3537–50.
[18] Mohammadshahi Shahrzad S, Gould Tim, Gray Evan MacA, Webb Colin J. An improved model for metal-hydrogen storage tanks–Part 2: model results. Int J Hydrogen Energy 2016;41(6):3919–27.
[19] Hardy BJ, Anton DL. Hierarchical methodology for modeling hydrogen storage systems. Part II: detailed models. Int J Hydrogen Energy 2009;34(7):2992–3004.
[20] Mohammadshahi SS, Webb TA, Gray E MacA, Webb CJ. Experimental and theoretical study of compositional inhomogeneities in $LaNi_5D_x$ owing to temperature gradients and pressure hysteresis, investigated using spatially resolved in-situ neutron diffraction. Int J Hydrogen Energy 2017;42(10):6793–800.
[21] Kyoung S, Ferekh S, Gwak G, Jo A, Ju H. Three-dimensional modeling and simulation of hydrogen desorption in metal hydride hydrogen storage vessels. Int J Hydrogen Energy 2015;40(41):14322–30.
[22] Sekhar BS, Lototskyy M, Kolesnikov A, Moropeng ML, Tarasov BP, Pollet BG. Performance analysis of cylindrical metal hydride beds with various heat exchange options. J Alloy Comp 2015;645(Suppl. 1):S89–95.
[23] Darzi AR, Afrouzi HH, Moshfegh A, Farhadi M. Absorption and desorption of hydrogen in long metal hydride tank

equipped with phase change material jacket. Int J Hydrogen Energy 2016;41(22):9595–610.
[24] Valizadeh M, Delavar MA, Farhadi M. Numerical simulation of heat and mass transfer during hydrogen desorption in metal hydride storage tank by Lattice Boltzmann method. Int J Hydrogen Energy 2016;41(1):413–24.
[25] Chung CA, Chen Y, Chen Y, Chang M. CFD investigation on performance enhancement of metal hydride hydrogen storage vessels using heat pipes. Appl Therm Eng 2015;91:434–46.
[26] Minko KB, Artemov VI, Yan'kov GG. Numerical study of hydrogen purification using metal hydride reactor with aluminium foam. Appl Therm Eng 2015;76:175–84.
[27] Mazzucco A, Rokni M. Generalized computational model for high-pressure metal hydrides with variable thermal properties. Int J Hydrogen Energy 2015;40(35):11470–7.
[28] Madaria Y, Kumar EA, Murthy SS. Effective thermal conductivity of reactive packed beds of hydriding materials. Appl Therm Eng 2016;98:976–90.
[29] Cho Ju, Yu S, Kim M, Kang S, Lee Y, Ahn K, et al. Dynamic modeling and simulation of hydrogen supply capacity from a metal hydride tank. Int J Hydrogen Energy 2013;38(21):8813–28.
[30] Krokos CA, Nikolic D, Kikkinides ES, Georgiadis MC, Stubos AK. Modeling and optimization of multi-tubular metal hydride beds for efficient hydrogen storage. Int J Hydrogen Energy 2009;34(22):9128–40.
[31] Wang Y, Adroher XC, Chen J, Yang XG, Miller T. Three-dimensional modeling of hydrogen sorption in metal hydride hydrogen storage beds. J Power Sources 2009;194(2):997–1006.
[32] Ma J, Wang Y, Shi S, Yang F, Bao Z, Zhang Z. Optimization of heat transfer device and analysis of heat & mass transfer on the finned multi-tubular metal hydride tank. Int J Hydrogen Energy 2014;39(25):13583–95.
[33] Ortmann Jerome P, Kaisare Niket S. Modeling of cryo-adsorption of hydrogen on MOF-5 pellets: effect of pellet properties on moderate pressure refueling. Int J Hydrogen Energy 2016;41(1):342–54.
[34] Jiao K, Li X, Yin Y, Zhou Y, Yu S, Du Q. Effects of various operating conditions on the hydrogen absorption processes in a metal hydride tank. Appl Energy 2012;94:257–69.
[35] Jemni A, Nasrallah SB, Lamloumi J. Experimental and theoretical study of ametal–hydrogen reactor. Int J Hydrogen Energy 1999;24(7):631–44.
[36] Demircan A, Demiralp M, Kaplan Y, Mat MD, Veziroglu TN. Experimental and theoretical analysis of hydrogen absorption in $LaNi_5$–H_2 reactors. Int J Hydrogen Energy 2005;30(13):1437–46.
[37] Momen G, Hermosilla G, Michau A, Pons M, Firdaouss M, Hassouni K. Hydrogen storage in an activated carbon bed: effect of energy release on storage capacity of the tank. Int J Hydrogen Energy 2009;34(9):3799–809.
[38] Muthukumar P, Singhal A, Bansal GK. Thermal modeling and performance analysis of industrial-scale metal hydride based hydrogen storage container. Int J Hydrogen Energy 2012;37(19):14351–64.
[39] Mahmut D, Mat Kaplan Y. Numerical study of hydrogen absorption in an Lm–Ni 5 hydride reactor. Int J Hydrogen Energy 2001;26(9):957–63.
[40] Maeda T, Nishida K, Tange M, Takahashi T, Nakano A, Ito H, et al. Numerical simulation of the hydrogen storage with reaction heat recovery using metal hydride in the totalized hydrogen energy utilization system. Int J Hydrogen Energy 2011;36(17):10845–54.
[41] Mellouli S, Dhaou H, Askri F, Jemni A, Nasrallah SB. Hydrogen storage in metal hydride tanks equipped with metal foam heat exchanger. Int J Hydrogen Energy 2009;34(23):9393–401.
[42] Wijayanta AT, Nakaso K, Aoki T, Kitazato Y, Fukai J. Effect of pressure, composition and temperature characteristics on thermal response and overall reaction rates in a metal hydride tank. Int J Hydrogen Energy 2011;36(5):3529–36.
[43] Førde T, Næss E, Yartys VA. Modelling and experimental results of heat transfer in a metal hydride store during hydrogen charge and discharge. Int J Hydrogen Energy 2009;34(12):5121–30.
[44] Mazumdar S, Bhattacharyya S, Ramgopal M. Compressor driven metal hydride cooling systems—mathematical model and operating characteristics. Int J Refrig 2005;28(6):798–809.
[45] Laurencelle F, Goyette J. Simulation of heat transfer in a metal hydride reactor with aluminium foam. Int J Hydrogen Energy 2007;32(14):2957–64.
[46] Brown Tim M, Brouwer J, Samuelsen GS, Holcomb FH, King J. Accurate simplified dynamic model of a metal hydride tank. Int J Hydrogen Energy 2008;33(20):5596–605.
[47] Gambini M, Manno M, Vellini M. Numerical analysis and performance assessment of metal hydride-based hydrogen storage systems. Int J Hydrogen Energy 2008;33(21):6178–87.
[48] Fukai Y. The metal-hydrogen system: basic bulk properties. Springer Science & Business Media; 2006.
[49] Bahrami M, Yovanovich MM, Culham JR. Effective thermal conductivity of rough spherical packed beds. Int J Heat Mass Tran 2006;49(19):3691–701.
[50] Gusarov AV, Kovalev EP. Model of thermal conductivity in powder beds. Phys Rev B 2009;80(2):024202.
[51] Nakagawa T, Inomata A, Aoki H, Miura T. Numerical analysis of heat and mass transfer characteristics in the metal hydride bed. Int J Hydrogen Energy 2000;25(4):339–50.
[52] Marty P, Fourmigue JF, De Rango P, Fruchart D, Charbonnier J. Numerical simulation of heat and mass transfer during the absorption of hydrogen in a magnesium hydride. Energy Convers Manag 2006;47(20):3632–43.
[53] Van de Lagemaat J, Benkstein Kurt D, Frank Arthur J. Relation between particle coordination number and porosity in nanoparticle films: implications to dye-sensitized solar cells. J Phys Chem B 2001;105(50):12433–6.
[54] Bahrami M, Culham JR, Yovanovich MM. A scale analysis approach to thermal contact resistance. Conference A scale analysis approach to thermal contact resistance. American Society of Mechanical Engineers p. 337–48.
[55] Song S, Yovanovich MM. Explicit relative contact pressure expression-Dependence upon surface roughness parameters and Vickers microhardness coefficients. Conference Explicit relative contact pressure expression-Dependence upon surface roughness parameters and Vickers microhardness coefficients. p. 152.
[56] Atteberry JE, Agosta DS, Nattrass CE, Leisure RG, Jacob I, Bowman RC, et al. Temperature dependence of the elastic moduli of polycrystalline $LaAl_xNi_{5-x}$ and $LaSn_xNi_{5-x}$. J Alloy Comp 2004;376(1):139–44.
[57] Popov Valentin L. Contact mechanics and friction. Springer; 2010.
[58] Bahrami M, Yovanovich MM, Culham JR. Thermal joint resistances of nonconforming rough surfaces with gas-filled gaps. J Thermophys Heat Tran 2004;18(3):326–32.
[59] Ueoka K, Miyauchi S, Asakuma Y, Hirosawa T, Morozumi Y, Aoki H, et al. An application of a homogenization method to the estimation of effective thermal conductivity of a hydrogen storage alloy bed considering variation of contact conditions between alloy particles. Int J Hydrogen Energy 2007;32(17):4225–32.
[60] Matsushita M, Monde M, Mitsutake Y. Experimental formula for estimating porosity in a metal hydride packed bed. Int J Hydrogen Energy 2013;38(17):7056–64.
[61] Bird RB, Stewart WE, Lightfoot EN. Transport phenomena, rev. New York: Wiley; 2007.

[62] Christopher Robert H, Middleman Stanley. Power-law flow through a packed tube. Ind Eng Chem Fundam 1965;4(4):422–6.
[63] Bergman TL, Incropera FP, DeWitt DP, Lavine AS. Fundamentals of heat and mass transfer. John Wiley & Sons; 2011.
[64] Pons M, Dantzer P. Determination of thermal conductivity and wall heat transfer coefficient of hydrogen storage materials. Int J Hydrogen Energy 1994;19(7):611–6.
[65] Pons M, Dantzer P, Guilleminot JJ. A measurement technique and a new model for the wall heat transfer coefficient of a packed bed of (reactive) powder without gas flow. Int J Heat Mass Tran 1993;36(10):2635–46.
[66] Kallweit J, Hahne E. Effective thermal conductivity of metal hydride powders: measurement and theoretical modelling. Institut fiir Thermodynamik und Warmetechnik, Universitat Stuttgart; 1994.
[67] Sanitjai S, Goldstein RJ. Forced convection heat transfer from a circular cylinder in crossflow to air and liquids. Int J Heat Mass Tran 2004;47:4795–805.
[68] Whitaker S. Forced convection heat transfer correlations for flow in pipes, past flat plates, single cylinders, single spheres, and for flow in packed beds and tube bundles. AIChE J 1972;18:361–71.
[69] Sun D, Deng S. A theoretical model predicting the effective thermal conductivity in powdered metal hydride beds. Int J Hydrogen Energy 1990;15(5):331–6.
[70] Asakuma Y, Miyauchi S, Yamamoto T, Aoki H, Miura T. Homogenization method for effective thermal conductivity of metal hydride bed. Int J Hydrogen Energy 2004;29(2):209–16.
[71] Mordovin VP, Prokhorov AI, Kutsev SV, Kalmakova AV, Uzintsev OE, Kapranova AI, et al. Physicomechanical properties of the hydrogen-accumulating intermetallics $LaNi_5$ and TiFe and a $LaNi_5$-Al composite. Russ Metall 2010;2010(4):365–70.
[72] Joubert JM, Černý R, Latroche M, Percheron-Guégan A, Yvon K. Compressibility and thermal expansion of $LaNi_5$ and its substitutional derivatives ($LaNi_{5-x}Mx$; M=Mn, Al, Co). Intermetallics 2005;13(2):227–31.
[73] Mellouli S, Askri F, Dhaou H, Jemni A, Nasrallah SB. A study of the thermal behavior of a deformable metal-hydride bed. Int J Hydrogen Energy 2016;41(3):1711–24.
[74] Askri F, Salah MB, Jemni A, Nasrallah SB. Optimization of hydrogen storage in metal-hydride tanks. Int J Hydrogen Energy 2009;34(2):897–905.